4950 Chem. Mater. **2010,** *22,* 4950–4963
DOI:10.1021/cm101041a

CHEMISTRY OF MATERIALS
Article

Trimming Nanostructured Walls While Fluorinating their Surfaces: A Route to Making and Widening Pores of Nanoporous Materials and Efficient Catalysts

Cole T. Duncan,[§] Ankush V. Biradar,[†,‡] Sylvie Rangan,[⊥] Richard E. Mishler II,[†,‡] and Tewodros Asefa*,[†,‡]

[†]*Department of Chemistry and Chemical Biology, Rutgers, The State University of New Jersey, 610 Taylor Road, Piscataway, New Jersey 08854,* [‡]*Department of Chemical Engineering and Biochemical Engineering, Rutgers, The State University of New Jersey, 98 Brett Road, Piscataway, New Jersey 08854,* [§]*Department of Chemistry, Syracuse University, 111 College Place, Syracuse, New York 13244, and* [⊥]*Department of Physics and Astronomy, Rutgers, The State University of New Jersey, 136 Frelinghuysen Road, Piscataway, New Jersey 08854*

Received April 14, 2010. Revised Manuscript Received June 27, 2010

We report on the synthesis and characterization of highly ordered mesoporous fluorosilicas (OMFs) and nanoporous and corrugated fluorosilica nanospheres which contain 2.4−7.0 wt % F, corresponding to a loading of 1.3−3.7 mmol/g. Synthesis of these materials is carried out from parent mesoporous silicas (MCM-41 and SBA-15) and silica nanospheres under ambient conditions using dilute nonaqueous solutions of triethyloxonium tetrafluoroborate (Et_3OBF_4). As evidenced by nitrogen physisorption measurements, small angle powder X-ray diffraction (XRD), and transmission electron microscopy (TEM), fluorination of the mesostructures is accomplished with only minor alteration of the materials' overall order. Detailed compositional analyses before and after fluorination are carried out with the aid of FTIR spectroscopy and X-ray photoelectron spectroscopy (XPS) as well as elemental analysis proving the existence of silicon oxyfluoride species. FTIR studies show the appearance of new absorptions (730−750 cm^{-1}) upon fluorination corresponding to $[F_{6-n}Si(OH)_n]^{2-}$, $O_{4/2}SiF$ species or Si−O−Si stretches altered by the presence of nearby Si−F species as well as general broadening of the Si−O−Si asymmetric stretching region (1000−1200 cm^{-1}). XPS analyses exhibit two distinct F species observed at 690.5 and 687.6 eV corresponding to silicon oxyfluoride (SiOF) and silicon fluoride (SiF), respectively. Surface silanol content is evaluated by ^{29}Si HP-MAS NMR spectroscopy, which shows significant reductions in $(Q^2+Q^3)/Q^4$ ratios from 1.26, 0.61, and 1.07 to 0.22, 0.38, and 0.61 for SBA-15, trimethylsilyl-capped SBA-15, and MCM-41 mesoporous silicas, respectively, because of the formation of $(SiO_3)\mathit{Si}F$ or pentacoordinated $(SiO_4)\mathit{Si}F$ species. The as-described synthetic procedure is also applied to sulfonic acid ($-SO_3H$)-functionalized SBA-15. Enhancement of the acid-catalyzed ring opening of styrene oxide by aniline to produce the corresponding β-aminoalcohol by the fluorinated materials is presented. Ring opening of styrene oxide by aniline at room temperature after 4 h using $-SO_3H$ functionalized SBA-15 result in 77% conversion, whereas the as-synthesized OMF and OMF-SO_3H materials exhibit 79% and 87% conversions, respectively. Fluorination of silica nanospheres with Et_3OBF_4 under similar conditions also produces etched nanoporous fluorosilica nanospheres with different degrees of exfoliation depending on the fluorination temperature.

1. Introduction

In recent years, there have been many significant developments toward the fabrication of silica-based nanoscale materials such as functionalized mesoporous silicates (FMS), functionalized SiO_2 nanospheres, and a plethora of core−shell nanomaterials with a wide range of physical and chemical properties for various applications.[1,2] Many of these materials contain procedural elements which include etching steps which partially dissolve silica from the material to increase surface area or enhance adsorptive capabilities while other methodologies aim to totally remove the silica to form novel metal oxides with unique structural properties such as in the formation hollow metal oxide nanospheres,[3] nanowires or nanotubes,[4] or mesoporous materials[5] where the silica was used as a scaffold. Solution phase silica etching has been widely reported to be accomplished by the use of either a concentrated strong base (i.e., KOH or NaOH) or by hydrofluoric acid (HF), which must be handled with extreme care due to inherent risks they impose during experimentation. These harsh etching techniques form soluble H_2SiF_6 or M_2SiO_3 (M = Na, K) salts, which are removed in the

---

*Corresponding author. Tel: (732) 445-2970. Fax: (732) 445-5312. E-mail: tasefa@rci.rutgers.edu.

(1) Asefa, T.; Anan, A.; Duncan, C. T.; Xie, Y. In *Non-Magnetic Bi-Metallic and Metal Oxide Nanomaterials for Life Sciences*; Kumar, C. S. S. R., Ed.; Wiley-VCH: Weinheim, Germany, 2009; Vol. *3*, Chapter 9.

(2) (a) Yang, Q.; Liu, J.; Zhang, L.; Li, C. *J. Mater. Chem.* **2009**, *19*, 1945–1955. (b) Huang, S.; Fan, Y.; Cheng, Z.; Kong, D.; Yang, P.; Quan, Z.; Zhang, C.; Lin, J. *J. Phys. Chem. C* **2009**, *113*, 1775–1784. (c) Gao, Q.; Xu, Y.; Wu, D.; Li, X. *J. Phys. Chem. C* **2009**, *113*, 12753–12758. (d) Vallet-Regí, M.; Balas, F.; Arcos, D. *Angew. Chem., Int. Ed.* **2007**, *46*, 7548–7558. (e) Hoffman, F.; Cornelius, M.; Morell, J.; Fröba, M. *Angew. Chem., Int. Ed.* **2006**, *45*, 3216–3251. (f) De Palma, R.; Peeters, S.; Van Bael, M. J.; Van den Rul, H.; Bonroy, K.; Laureyn, W.; Mullens, J.; Borghs, G.; Maes, G. *Chem. Mater.* **2007**, *19*, 1821–1831.

(3) Pan, J. H.; Zhang, X.; Du, A. J.; Sun, D. D.; Leckie, J. O. *J. Am. Chem. Soc.* **2008**, *130*, 11256–11257.

washing procedure leaving the remaining etched silica. As will be discussed, there are also many examples where fluorine containing species, such as ionic liquids or gaseous mixtures, have been utilized as etching and fluorinating agents. Such methodologies produce a substantial amount of fluoride ions which, when in the presence of a silica species, lead to the formation of insoluble fluorosilicate or organofluorosilicate species. The fabrication of such materials has been studied extensively as useful components of low dielectric (*k*) microelectronic devices.[6] Fluorinated silicas have also found utility in amide dehydration reactions[7] and alkylation reactions.[8]

The synthesis of fluoro- and organofluoro-silicate species has been accomplished using a variety of different methodologies. For example, the fabrication of thin films via plasma-enhanced chemical vapor deposition (PECVD), using gaseous mixtures consisting of fluorine containing species such as SiF_4, C_4F_8, or SF_6, oxygen (O_2), inert gases such as Ar or He, and a silica source [i.e., Si(100) substrates, tetraethylorthosilicate (TEOS) or trimethylsilane (TMS)] has shown to result in potential fluorosilicate species useful for low *k* devices.[9] Fabrication using PECVD requires careful manipulation of reagent ratios by varying gas flow rate during deposition producing thin films with reported F content ranging from 2−25 at %. Direct fluorination of mesoporous silica gel using F_2 gas has also been proven to produce F containing materials with 4−13 wt % F (2.1−6.8 mmol/g) without the formation of unwanted SiF_4 or SiF_6^{2-} species. However, the latter synthetic method involving F_2 gas significantly reduces the surface area (14−46%) of the parent material and is extremely dangerous, necessitating highly specialized equipment that may inhibit broad application.[10]

Other procedures utilize aqueous or nonaqueous fluoride containing salt solutions to etch and/or fluorinate silica. For instance, dilute NH_4F in aqueous media has been shown to promote the formation of Si−F species via nucleophilic substitution of surface silanols.[11] This procedure, however, generates species with relatively low fluorine contents of 0.7−1.6 wt % (0.4−0.8 mmol/g) whereas higher fluorine content is due to the formation of $(NH_4)_2SiF_x(OH)_{6-x}$ salts as evidenced by ^1H high-spinning frequency MAS NMR spectroscopy.[12] Tetrafluoroborate (BF_4^-), hexafluorophosphate (PF_6^-), and other similar ionic liquids (ILs) have also been used to produce F^- ions in situ in a slow and controlled fashion. For example, the dissociation of tetrafluoroborate (eq 1) has a significantly low dissociation constant (*K*);[13] however, because of the high affinity that silicon has for fluoride ion, fluoride ion is rapidly quenched resulting in an equilibrium shift to the right.

$$BF_4^-(aq) \leftrightarrow BF_3(aq) + F^-(aq) \quad K = 1 \times 10^{-39} \qquad (1)$$

Using this motif, 1-hexyl-3-methyl-imidazolium, 1-butyl-4-methyl-pyridinium, and tetrabutylammonium BF_4^-/PF_6^- compounds were used in the etching and growth of InP nanocrystals by microwave induction.[14] Similar fluorine-containing ILs have also been shown to be a suitable alternative to HF for electrochemically and photoelectrochemically induced etching of n-type and p-type silicon wafers.

On the other hand, although there are many examples of fluorinated nanoscale low *k* materials, the use of fluorinated and/or functionalized fluorinated silicates in catalysis is still relatively uncharted. One property of interest relating to the fluorination of silicates or aluminosilicates is the enhancement of surface acid catalyzed reactions. Recently, the dealumination of the zeolite ferrierite using ammonium hexafluorosilicate $(NH_4)_2SiF_6$ yielded a fluorinated zeolite that exhibited selectivity in the skeletal isomerization of *n*-butene to isobutene.[15] Ammonia temperature programmed desorption (TPD) and pyridine chemisorption studies showed the surface acidity was reduced because of the fluorination of mainly the stronger acid sites. This, in turn, led to a lower surface density of acid sites, which lowered the possibility of competing active sites and reduced the local reagent concentration, thus inhibiting the formation of unwanted byproducts. Although the fluorinated materials exhibited a

---

(4) (a) Arnold, D. C.; O'callaghan, J. M.; Sexton, A.; Tobin, J. M.; Amenitsch, H.; Holmes, J. D.; Morris, M. A. *Appl. Surf. Sci.* **2009**, *255*, 9333–9342. (b) Megouda, N.; Hadjersi, T.; Piret, G.; Boukherroub, R.; Elkechai, O. *Appl. Surf. Sci.* **2009**, *255*, 6210–6216. (c) Douani, R.; Hadjersi, T.; Boukherroub, R.; Adour, L.; Manseri, A. *Appl. Surf. Sci.* **2008**, *254*, 7219–7222. (d) Asefa, T.; Shi, Y.-L. *J. Mater. Chem.* **2008**, *18*, 5604–5614. (e) Ge, J.; Zhang, Q.; Zhang, T.; Yin, Y. *Angew. Chem., Int. Ed.* **2008**, *47*, 8924–8928. (f) Mulvihill, M. J.; Rupert, B. L.; He, R.; Hochbaum, A.; Arnold, A.; Yang, P. *J. Am. Chem. Soc.* **2005**, *127*, 16040–16041. (f) Whitsitt, E. A.; Barron, A. R. *Nano Lett.* **2003**, *3*, 775–778.

(5) Yan, J.; Wang, A.; Kim, D.-P. *J. Phys. Chem. B* **2006**, *110*, 5429–5433.

(6) (a) Cardinaud, C.; Peignon, M.-C.; Tessier, P.-Y. *Appl. Surf. Sci.* **2000**, *164*, 72–83. (b) Mocella, M. T. *J. Fluorine Chem.* **2003**, *122*, 87. (c) Urbansky, E. T. *Chem. Rev.* **2002**, *102*, 2837–2854. (d) Katsuo, T.; Satohito, Y.; Kimio, T. *Bull. Jpn. Pet. Inst.* **1970**, *12*, 136–141.

(7) Jacques, R.; Reppelin, M.; Seigneurin, L. Fluorinated silica catalyst and preparation of aromatic/aliphatic nitriles in the presence thereof. U.S. Patent 4 822 903, May 27, 2006.

(8) (a) Mantilla-Ramírez, A.; Ferrat-Torres, G.; Domínguez, J. M.; Aldana-Rivero, C.; Bernal, M. *Appl. Catal., A* **1996**, *143*, 203–214. (b) Han, S.; Shihabi, D. S.; Chang, C. D. *J. Catal.* **2000**, *196*, 375–378. (c) Cañizares, P.; Carrero, A. *Appl. Catal., A* **2003**, *248*, 227–237.

(9) (a) Pankov, V.; Alonso, J. C.; Ortiz, A. *J. Appl. Phys.* **1999**, *86*, 275–280. (b) Wang, P.-F.; Ding, S.-J.; Zhang, W.; Zhang, J.-Y.; Wang, J.-T.; Wei, W.-L. *Chin. Phys. Lett.* **2000**, *17*, 912–914. (c) Kim, S. P.; Choi, S. K. *Thin Solid Films* **2000**, *379*, 259–264. (d) Wang, P.-F.; Ding, S.-J; Zhang, D. W.; Wang, J.-T.; Lee, W. W. *Thin Solid Films* **2001**, *385*, 115–119. (e) Park, Y.-B.; Rhee, S.-W. *J. Non-Cryst. Solids* **2004**, *343*, 33–38. (f) Cheng, Y. L.; Wang, Y. L.; Juang, Y.; O'Neill, M. L.; Lukas, A. S.; Karwacki, E. J.; McGuian, S. A.; Tang, A.; Wu, C. L. *J. Phys. Chem. Solids* **2008**, *69*, 518–522. (g) Pereira, J.; Pichon, E.; Dussart, R.; Cardinaud, C.; Duluard, C. Y.; Oubensaid, E. H.; Lefaucheux, P.; Boufnichel, M.; Ranson, P. *Appl. Phys. Lett.* **2009**, *94*, 071501–071503.

(10) (a) Lataste, E.; Legein, C.; Body, M.; Buzaré, J.-Y.; Tressaud, A.; Demourgues, A. *J. Phys. Chem. C* **2009**, *113*, 18652–18660. (b) Lataste, E.; Demourgues, A.; Leclerc, H.; Goupil, J.-M.; Durand, E.; Labrugère, C.; Benalla, H.; Tressaud, A. *J. Phys. Chem. C* **2008**, *112*, 10943–10951.

(11) (a) Jungblut, H.; Lewerenz, H. J. *Appl. Surf. Sci.* **2000**, *168*, 194–197. (b) Loius, B.; Kiwi-Minsker, L. *Microporous Mesoporous Mater.* **2004**, *74*, 1–10. (c) Hartmeyer, G.; Marichal, C.; Lebeau, B.; Caullet, P.; Hernandez, J. *J. Phys. Chem. C* **2007**, *111*, 6634–6644. (d) Barabash, R. M.; Zaitsev, V. N.; Kovalchuk, T. V.; Sfihi, H.; Fraissard, J. *J. Phys. Chem. A* **2003**, *107*, 4497–4505.

(12) Hartmeyer, G.; Marichal, C.; Lebeau, B.; Rigolet, S.; Caullet, P.; Hernandez, J. *J. Phys. Chem. C* **2007**, *111*, 9066–9071.

(13) Stacey, M.; Tatlow, J. C.; Sharpe, A. G. In *Advances in Fluorine Chemistry*; Academic Press: New York, 1960; Vol. *1*, p 72.

(14) Lovingood, D. D.; Strouse, G. F. *Nano Lett.* **2008**, *8*, 3394–3397.

(15) Cañizares, P.; Carrero, A. *Appl. Catal., A* **2003**, *248*, 227–248.

lower % conversion, they reduced the formation of byproducts such as propane and *n*-butane. The oligomerization of propene was also studied using an $(NH_4)_2SiF_6$ treated zeolite HZSM-5.[16] The formation of unbranched C_{20}^+ hydrocarbons was enhanced upon fluorination compared to that of the nonfluorinated zeolite. Additionally, the formation of unwanted branched oligomers was reduced. The fluorinated materials were shown to have isolated acidic sites and lowered surface acidity than that of the parent material, and result in limited oligomer branching. Sulphated TiO_2-SiO_2 mixed oxide species that could be used as a Brønsted acid catalyst for cumene cracking and esterification reactions showed increased reactivity upon fluorination.[17] Fluorination was accomplished using a solution of NH_4F in dilute sulfuric acid resulting in materials with 0.5−2 wt % F (0.3−1.1 mmol/g) and enhanced catalytic activity because of higher Brønsted acidity and favorable inductive interactions with nearby SO_4^{2-}.

Herein, we report on the synthesis of mesoporous SBA-15 and MCM-41 type highly ordered mesoporous fluorosilicas (OMFs) and nanoporous and corrugated fluorosilica nanospheres (CFNSs) using triethyloxonium tetrafluoroborate (Et_3OBF_4), a commonly used alkylating agent in organic syntheses. Using facile synthetic protocols, OMFs and CFNSs were prepared without the use of HF, toxic gas mixtures, or specialized equipment necessary for electrochemical, PECVD or microwave induced procedures. Although many of the other procedures mentioned use either silica wafers or as-synthesized thin layers, this procedure is capable of producing OMF's on a large scale. The composition of synthesized OMF species were examined via FTIR spectroscopy, X-ray photoelectron spectroscopy (XPS), and elemental and thermogravimetric (TGA) analyses and found to contain 2.4−7.0 wt % F corresponding to a loading of 1.3−3.7 mmol/g. The morphology of the materials was investigated using nitrogen physisorption measurements, small angle powder X-ray diffraction (XRD), transmission electron microscopy (TEM), and solid state ^{29}Si HP-MAS and CP-MAS NMR spectroscopy. This synthetic method enables widening and restructuring of the pore diameters of mesoporous silica without compromising its ordered structure while at the same time permitting fluorination of the material's surface. Fluorinated materials exhibit larger pore volumes and diameters with only minor resultant pore constriction. To further study the effects of our presented fluorination methodology, we assessed the catalytic activity of OMF and sulfonic-acid-functionalized mesoporous fluorosilica materials (OMF-SO_3H) in the ring opening of styrene oxide by aniline forming the corresponding β-amino alcohol and compared it to that of the corresponding nonfluorinated materials. β-Amino alcohols have shown promise as biological/medicinal agents or chiral auxiliaries,[18] insecticides,[19] and metal chelates in catalysis.[20] To date, several methodologies have been shown to catalytically form β-amino alcohols from epoxides and aromatic/aliphatic amines. Metal halides,[21] triflates,[22] nitrates[23] and perchlorates,[24] sulfamic acid,[25] hexafluoro-2-propanol (HFIP),[26] 1,4-diazabicyclic[2,2,2]-octane (DABCO),[27] ionic liquids,[28] and even water[29] have all been shown capable of catalyzing the ring opening reaction of epoxides by amines. Heterogeneous catalysts, such as aluminosilicates,[30] functionalized and non-functionalized mesoporous silicas,[31] polyoxometalates,[32] silica and titanosilicate nanoparticles,[33] amberlyst-15,[34]

---

(16) (a) Han, S.; Shihabi, D. S.; Chang., C. D. *J. Catal.* **2000**, *196*, 375–378.

(17) Samantaray, S. K.; Parida, K. M. *Appl. Catal., A* **2001**, *211*, 175–187.

(18) (a) Córdova, I.; León, L. G.; León, F.; San Andres, L.; Luis, J. G.; Padrón, J. M. *Eur. J. Med. Chem.* **2006**, *41*, 1327–1332. (b) Clarkson, C.; Musonda, C. M.; Chibale, K.; Campbell, W. E.; Smith, P. *Bioorg. Med. Chem.* **2003**, *11*, 4417–4422. (c) Danieli, E.; Trabocchi, A.; Menchi, G.; Guarna, A. *Eur. J. Org. Chem.* **2005**, 4372–4381. (d) Ager, D. J.; Prakash, I.; Schaad, D. R. *Chem. Rev.* **1996**, *96*, 835–875.

(19) (a) Ferrarini, S. R.; Duarte, M. O.; da Rosa, R. G.; Rolim, V.; Eifler-Lima, Gilsane von Poser, V. L.; Sardá Ribeiro, V. L. *Vet. Parasitol.* **2008**, *157*, 149–153. (b) Graebin, C. S.; Madeira, M; Yokoyama-Yasunaka, J. K. U.; Miguel, D. C.; Uliana, S. R. B.; Benitez, D.; Cerecetto, H.; Mercedes González, M.; Gomes da Rosa, R.; Eifler-Lima, V. L. *Eur. J. Med. Chem.* **2010**, *45*, 1524–1528.

(20) (a) Yan, W.; Mao, B.; Zhu, S.; Jiang, X.; Liu, Z.; Wang., R. *Eur. J. Org. Chem.* **2009**, 3790–3794. (b) Zhu, S.; Yan, W.; Mao, B.; Jiang, X.; Wang, R. *J. Org. Chem.* **2009**, *74*, 6980–6985. (c) Mahadik, G. S.; Knott, S. A.; Szczepura, L. F.; Peters, S. J.; Standard, J. M.; Hitchcock, S. R. *J. Org. Chem.* **2009**, *74*, 8164–8173. (d) Dahlenburg, L.; Treffert, H.; Farr, C.; Heinemann, F. W.; Zahl, A. *Eur. J. Inorg. Chem.* **2007**, 1738–1751. (e) Li, Y.; He, B.; Qin, B.; Feng, X.; Zhang, G. *J. Org. Chem.* **2004**, *69*, 7910–7913. (f) Rasmussen, T.; Norrby, P. *J. Am. Chem. Soc.* **2003**, *125*, 5130–5138.

(21) (a) Mojtahedi, M. M.; Abaee, M. S.; Hamidi, V. *Catal. Commun.* **2007**, *8*, 1671–1674. (b) Chakraborti, A. K.; Rudrawar, S.; Kondaskar, A. *Eur. J. Org. Chem.* **2004**, 3597–3600. (c) Sundararajan, G.; Vijayakrishna, K.; Varghese, B. *Tetrahedron Lett.* **2004**, *45*, 8253–8256. (d) Pachón, L. D.; Gamez, P.; van Brussel, J. J. M.; Reedijk, J. *Tetrahedron Lett.* **2003**, *44*, 6025–6027. (e) Chakraborti, A. K.; Kondaskar, A. *Tetrahedron Lett.* **2003**, *44*, 8315–8319.

(22) (a) Procopio, A.; Gaspari, M.; Nardi, M.; Oliverio, M.; Rosati, O. *Tet. Lett.* **2008**, *49*, 2289–2293. (b) Placzek, A. T.; Donelson, J. L.; Trivedi, R. *Tetrahedron Lett.* **2005**, *46*, 9029–9034. (c) Gibbs, R. A.; De, S. K. *Chem. Lett.* **2004**, *33*, 304–305.

(23) Bhanushali, M. J.; Nandurkar, N. S.; Bhor, M. D.; Bhanage, B. M. *Tetrahedron Lett.* **2008**, *49*, 3672–3676.

(24) Pujala, S. B.; Chakraborti., A. K. *J. Org. Chem.* **2007**, *72*, 3713–3722.

(25) Kamal, A.; Rajendra Prasad, B.; Malla Reddy, A.; Naseer, M.; Khan, A. *Catal. Commun.* **2007**, *8*, 1876–1880.

(26) Das, U.; Crousse, B.; Kesavan, V.; Bonnet-Delpon, D.; Begue, J. P. *J. Org. Chem.* **2000**, *65*, 6749–6751.

(27) Wu, J.; Xia, H. G. *Green Chem.* **2005**, *7*, 708–710.

(28) Yadav, J. S.; Reddy, B. V. S.; Basak, A. K.; Narsaiah, A. V. *Tet. Lett.* **2003**, *44*, 1047–1050.

(29) (a) Wang, Z.; Cui, Y. T.; Xu, Z. B.; Qu., J. *J. Org. Chem.* **2008**, *73*, 2270–2274. (b) Bonollo, S.; Fringuelli, F.; Pizzo, F.; Vaccaro, L. *Green Chem.* **2006**, *8*, 960–964. (c) Azizi, N.; Saidi, M. R. *Org. Lett.* **2005**, *7*(17), 3649–3651.

(30) (a) Kureshy, R. I.; Agrawal, S.; Kumar, M.; Khan, N. H.; Abdi, S. H. R.; Bajaj, H. C. *Catal. Lett.* **2010**, *134*, 318–323. (b) Chakravarti, R.; Oveisi, H.; Kalita, P.; Pal, R. R.; Halligudi, S. B.; Kantam, M. L.; Vinu, A. *Microporous Mesoporous Mater.* **2009**, *123*, 338–344. (c) Robinson, M. W. C.; Timms, D. A.; Williams, S. M.; Graham, A. E. *Tetrahedron Lett.* **2007**, *48*, 6249–6251. (d) Kureshy, R. I.; Singh, S.; Khan, N. H.; Abdi, S. H. R.; Suresh, E.; Jasra, R. V. *J. Mol. Catal., A* **2007**, *264*, 162–169. (e) Onaka, M.; Kawai, M.; Izumi, Y. *Chem. Lett.* **1985**, 779–782.

(31) (a) Bordoloi, A.; Hwang, Y. K.; Hwang, J. S.; Halligudi, S. B. *Catal. Commun.* **2009**, *10*, 1398–1403. (b) Heravi, M. M.; Baghernejad, B.; Oskooie, H. A. *Catal. Lett.* **2009**, *130*, 547–550. (c) Saikia, L.; Satyarthi, J. K.; Srinivas, D.; Ratnasamy, P. *J. Catal.* **2007**, *252*, 148–160.

(32) Danafar, H.; Yadollahi, B. *Catal. Commun.* **2009**, *10*, 842–847.

(33) (a) Sreedhar, B.; Radhika, P.; Neelima, B.; Hebalkar, N. *J. Mol. Cat. A: Chem.* **2007**, *272*, 159–163. (b) Satyarthi, J. K.; Saikia, L.; Srinivas, D.; Ratnasamy, P. *Appl. Catal., A* **2007**, *330*, 145–151.

(34) Vijender, M.; Kishore, P.; Narender, P.; Satyanarayana, B. *J. Mol. Catal., A* **2007**, *266*, 290–293.

and sulfated zirconia[35] have also been used as catalysts for the epoxide ring-opening reaction. Many of these catalysts, however, suffer from extended reaction times, elevated temperatures, large amounts of catalyst, or assistance of a solvent to perform efficiently. Herein, we also report on the use of OMF's as solid acid catalysts for the formation of β-amino alcohols. The fluorination methodology outlined in this paper was applied to the fluorination SBA-15 and sulfonic acid functionalized SBA-15 catalysts. The outlined catalytic procedure is solvent-free and does not require elevated temperatures, which is necessary to prevent the formation of unwanted byproducts and to avoid the loss or degradation of organic materials functionalized on the surface.[9d] This fluorination and etching method has also been proven to be versatile as it also allows etching of nanosized silica spheres of ~250−300 nm producing corrugated nanoporous fluorosilica nanospheres (CFSNs). This new method may serve as a facile route for tuning structures and fluorinating surfaces of a wide range of nanostructured and nanoporous metal oxides as well as provide a method for improved preparation of functionalized mesoporous silicates or similar nanoscale materials and nanocatalysts.

2. Experimental Section

Materials and Reagents. All reactions were performed under standard atmospheric conditions. Ethanol (EtOH, 95%) was obtained from Pharmco-AAPER. Aniline (≥99.5%), dichloromethane (CH_2Cl_2, ≥99.5%) hexamethyldisilazane (≥99%), styrene oxide (97%), tetraethyl orthosilicate (98%) (TEOS), toluene (≥99.5%), and triethyloxonium tetrafluoroborate (Et_3OBF_4, 1.0 M in CH_2Cl_2) were purchased from Sigma-Aldrich. 3-Mercaptopropyltrimethoxysilane (MPTS) was purchased from Gelest. Hydrochloric acid (12.1 N), sulphuric acid (36 N), and H_2O_2 (30 wt %) were obtained from Fisher Scientific. All the chemicals were used as received.

Synthesis of SBA-15 and MCM-41 Mesoporous Silica Materials. Synthesis of mesoporous SBA-15 and surfactant extraction via solvent washing was performed as reported in previously published literature.[36] Synthesis of mesoporous MCM-41 and surfactant extraction via calcination at 550 °C for 5 h was performed as reported previously.[37]

Synthesis of Organic Capped SBA-15 (CSBA-15). A solution of extracted SBA-15 (1.0 g) in toluene (200 mL) was prepared. Excess hexamethyldisilazane (HMDS, 5 mL) was added to the solution and allowed to stir at room temperature for 24 h as performed previously.[38] The solution was filtered and the solid was washed with ethanol and then dried. The resulting trimethylsilyl-capped sample was named as CSBA-15.

Synthesis of 250 nm Silica Nanospheres (NS). A solution of ethanol (100 mL) and water (3.6 g) was stirred vigorously for 2 min. TEOS (2.8 g) was then added into it under moderate stirring. After 3 h of stirring, a milky solution was formed. The solution was centrifuged and the supernatant was carefully decanted. The precipitate was washed three times with a solution of deionized (DI) H_2O (20 mL) and ethanol (20 mL) under sonication. The precipitate was dispersed in a 1:1 water/ethanol solution (40 mL overall) until further use. The resulting silica nanospheres (NS) were found by TEM to be 250 ± 10 nm in diameter.

Etching and Fluorination of Mesoporous Materials. Typically, mesoporous silica (0.2 g) was dispersed in CH_2Cl_2 (100 mL). 1.0 M Et_3OBF_4 (1.5−6 mL) was then added and the solution was allowed to stir for 19 h at room temperature or under reflux (50 °C). Upon completion, the mesoporous silica was recovered via vacuum filtration and washed with CH_2Cl_2 (200 mL) and EtOH (200 mL). The material was dried overnight at 80 °C and stored in a desiccator for future analysis. This experiment was performed on MCM-41, SBA-15 and CSBA-15. Furthermore, different concentrations: low (1.5×10^{-2} M), medium (2.9×10^{-2} M), and high (5.7×10^{-2} M) concentrations of Et_3OBF_4 and different etching temperatures of room temperature (RT) and 50 °C were used in each case. The resulting etched samples were given designations based on the etching condition employed (etching temperature and concentration). For instance, SBA-15 samples after etching at RT in low (1.5×10^{-2} M), medium (2.9×10^{-2} M), and high (5.7×10^{-2} M) concentrations of Et_3OBF_4 were designated as SBA-L-RT, SBA-M-RT, and SBA-H-RT, respectively, where L, M, and H stand for low, medium, and high, respectively. Similarly, SBA-15 samples after etching at 50 °C in low, medium, and high concentrations of Et_3OBF_4 were designated as SBA-L-50, SBA-M-50, and SBA-H-50, respectively. Similar sample designation was also applied for the MCM-41, CSBA-15, and silica nanospheres.

Synthesis of Solid Acid Catalyst. Synthesis of sulfonic-acid-functionalized SBA-15 was carried out in a manner similar to previously reported procedures.[39] Briefly, as-synthesized SBA-15 was calcined at 550 °C for 5 h. SBA-15 (1.6 g) was dispersed in dry toluene. MPTS (2.2 mL, 11.8 mmol) was then added to the solution and stirred at 80 °C for 5 h. The MPTS-modified SBA-15 was then separated via vacuum filtration and washed copiously with EtOH (95%) and dried overnight at 80 °C. Oxidation of surface mercaptopropyl groups was performed by dissolving the material (0.6 g) in H_2O_2 (30 wt %, 20 mL) and stirring at RT for 24 h. The material was then separated via vacuum filtration and washed copiously with DI H_2O. The material was then resuspended in 60 mL of 1 M H_2SO_4 for 2 h to ensure complete oxidation. The formed sulfonic acid catalyst (SBA-15-SO_3H) was then separated via vacuum filtration and washed with 2 L DI H_2O followed by 500 mL EtOH (95%) and dried.

Fluorination of the as-synthesized solid acid catalyst was performed as above. SBA-15-SO_3H (0.200 g) was dispersed in CH_2Cl_2 (100 mL) via sonication. A 1.0 M Et_3OBF_4 solution (6 mL) was added via syringe and the reaction was stirred overnight at RT. The fluorinated solid acid catalyst (OMF-SO_3H) was separated via vacuum filtration and washed with CH_2Cl_2 (500 mL) and dried for 3 h at 80 °C and stored in a desiccator until further use.

Catalytic Experiments. Aniline (450 μL, 5 mmol) and styrene oxide (570 μL, 5 mmol) were combined in a 5 mL round-bottom

---

(35) Reddy, B. M.; Patil, M. K.; Reddy, B. T.; Park, S. E. *Catal. Commun.* **2008**, *9*, 950–954.

(36) Zhao, D. Y.; Huo, Q. S.; Feng, J. L.; Chmelka, B. F.; Stucky, G. D. *J. Am. Chem. Soc.* **1998**, *120*, 6024–6036.

(37) Kresge, C. T.; Leonowicz, M. E.; Roth, W. J.; Vartuli, J. C.; Beck, J. S. *Nature* **1992**, *359*, 710–712.

(38) (a) McKittrick, M. W.; Jones, C. W. *Chem. Mater.* **2005**, *17*, 4758–4761. (b) Xie, Y.; Quinlivan, S.; Asefa, T. *J. Phys. Chem. C.* **2008**, *112*, 9996–10003.

(39) (a) Dhainaut, J.; Dacquin, J.; Lee, A. F.; Wilson, K. *Green Chem.* **2010**, *12*, 296–303. (b) Kureshy, R. I.; Ahmad, I.; Pathak, K.; Khan, N. H.; Abdi, S. H. R.; Jasra, R. V. *Catal. Commun.* **2009**, *10*, 572–575. (c) Reddy, S. S.; Raju, B. D.; Kumar, S.; V.; Padmasri, A. H.; Narayanan, S. K.; Rao, S. R. *Catal. Commun.* **2007**, *8*, 261–266. (d) Saikia, L.; Satyarthi, J. K.; Srinivas, D.; Ratnasamy, P. *J. Catal.* **2007**, *252*, 148–160.

flask. The catalyst (13 mg) was then added to the reaction mixture and dispersed via sonication. The reaction was vigorously stirred under ambient conditions. The reaction yields and compositions were monitored by gas chromatography (GC) and gas chromatography−mass spectrometry (GC-MS). The product was purified using column chromatography and analyzed via ^{1}H NMR. For 2-phenylamino-2-phenyl ethanol (Regioisomer B): ^{1}H NMR ($CDCl_3$, 300 MHz): δ 3.72 (1H, dd), 3.92 (1H, dd), 4.52 (1H, dd), 6.65 (2H, d), 6.79 (1H, t), 7.20 (2H, t), and 7.30−7.44 (5H, m). ^{13}C-NMR ($CDCl_3$, 300 MHz): δ 60.4, 67.7, 114.4, 118.4, 127.3, 128.0, 129.2, 129.7, 140.7, 141.1, 142.5, 147.9, 149.7. GC-MS (*m*/*e*): 214.1, 213.0, and 182.0.

Instrumentation. Solid-state ^{29}Si CP-MAS and HP-MAS NMR spectra were obtained using a 300 MHz Brüker Avance NMR spectrometer. For ^{29}Si CP-MAS NMR experiments, 7.0 kHz spin rate, 10 s recycle delay, 10 ms contact time, $\pi/2$ pulse width of 5.6 μs, and 256 − 1024 scans using TPPM ^{1}H decoupling were employed. ^{29}Si HP-MAS experiments were done with a 7.0 kHz spin rate, 100 s recycle delay, $\pi/6$ pulse width of 1.9 μs, and 700−4000 scans using high-power continuous-wave ^{1}H decoupling. Solution state ^{1}H and ^{13}C NMR spectra were obtained using a Brüker DPX-300 NMR. FTIR spectra were obtained using a Thermo-Nicolet IR200 spectrometer with samples loaded onto a KBr disk (25 × 4 mm). Thermogravimetric analysis (TGA) or decomposition profiles were acquired for mesoporous materials with a Q500 series thermogravimetric analyzer (TA Instruments). The TGA data were collected under nitrogen atmosphere (60 cm^3/min) in the temperature range of 25−800 °C at a rate of 10 °C/min. Gas adsorption isotherms were obtained using a Micromeritics Tristar 3000 surface area and porosity analyzer. Samples were degassed at 160 °C for 12−16 h and run at 77 K under nitrogen adsorption/desorption. The specific surface area (S_{BET}) was calculated according to the Brunauer−Emmett−Teller (BET) method from the adsorption branch of the isotherm. Pore size distributions were obtained using the Barrett−Joyner−Halenda (BJH) method from the adsorption branch of the N_2 sorption isotherm. Powder X-ray diffraction (XRD) profiles were obtained using a Scintag powder diffractometer. TEM images were taken with a FEI Tecnai T-12 S/TEM instrument. X-ray photoelectron spectroscopy (XPS) was performed using a Surface Science Instrument SSX-100. The reaction mixtures of catalytic studies were analyzed by GC (Agilent equipped with HP 6850, FID detector and HP-1, 30 m long × 0.25 mm ID column). The products were confirmed by GC-MS (HP-5971 equipped with a HP-5 MS 50 m long × 0.200 mm × 0.33 μm capillary column). Elemental analyses of all the materials were carried out by QTI-Intertek (Whitehouse, NJ).

3. Results and Discussion

The preparation of highly ordered OMFs was accomplished from SBA-15 and MCM-41 using Et_3OBF_4, a common alkylating agent in many organic syntheses. To study the effect of concentration and temperature, preparation was carried out in dilute Et_3OBF_4 solutions of 1.5, 2.9, and 5.7 × 10^{-2} M (in CH_2Cl_2), respectively, at room temperature (RT) and reflux (50 °C) under atmospheric conditions. These concentrations of Et_3OBF_4 were labeled as low (L), medium (M), and high (H) concentrations, respectively. The materials before and after fluorination with Et_3OBF_4 were characterized by nitrogen physisorption measurements, FT-IR spectroscopy, solid-state ^{29}Si NMR spectroscopy, TGA, TEM, powder XRD, XPS spectroscopy, and elemental analyses.

Scheme 1. Possible Mechanisms of Mesoporous Fluorosilicate Formation: (A) Fluorination of Surface Silanols via Nucleophilic Substitution and/or (B) Fluorination of the Fully Condensed Silica within the Mesoporous Framework

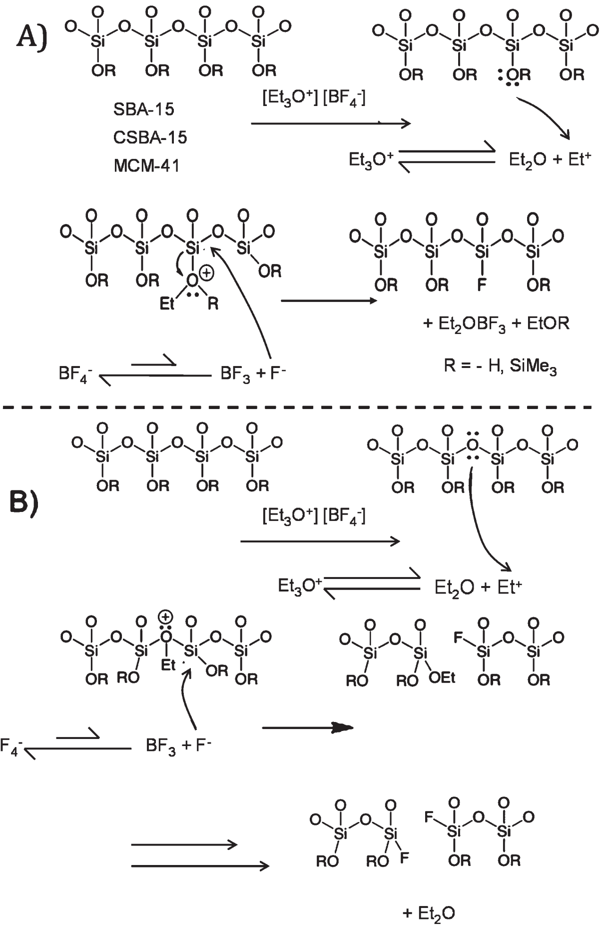

The fluorination process is believed to take place according to two different possible mechanisms shown in Scheme 1. These mechanisms are supported by detailed characterization methods such as solid-state ^{29}Si NMR, elemental analysis, FTIR and XPS which will be discussed in the proceeding sections. As shown in mechanism A of Scheme 1, the reaction is believed to be carried by the following steps: (1) formation of oxonium ion via introduction of Et$^+$, (2) nucleophilic attack by fluoride ion to silica surface, and (3) displacement of ethanol or, in the case of CSBA-15, ethoxytrimethylsilane. The coordination of F$^-$ and dissociation of EtOR (R = H or $SiMe_3$) most likely takes place through an associative mechanism with the formation of a pentavalent silicon species, which is the commonly accepted mechanism for substitution for silicon. The second possible route (mechanism B) shows a similar mechanism; however, in this case, formation of the oxonium ion occurs within the fully condensed silica framework. Upon nucleophilic attack of F$^-$, a corresponding ethoxysilane moiety is formed on the surface which may further react, as in mechanism A, to form another fluorosilica species and one equivalent of Et_2O. Because of the fact that fluorination occurs in a nonaqueous solvent,

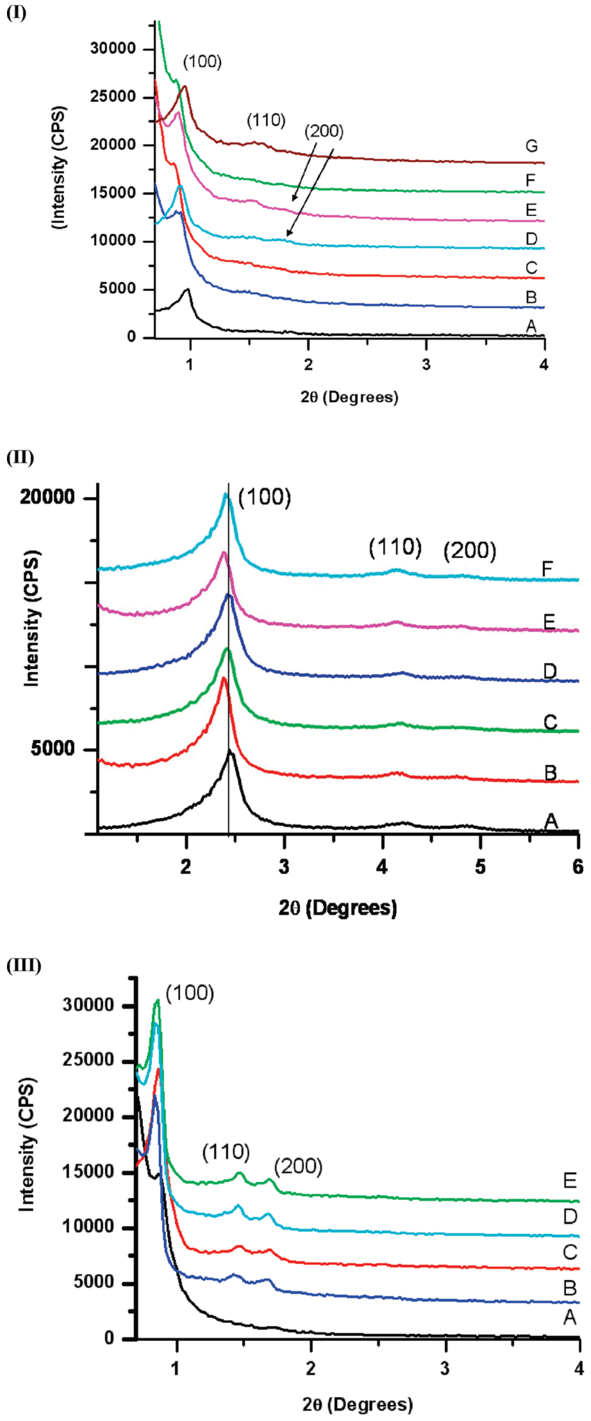

Figure 1. XRD patterns of (I) SBA-15 (A) before and (B−G) after fluorination under varying conditions: (B) SBA-L-RT, (C) SBA-M-RT, (D) SBA-H-RT, (E) SBA-L-50, (F) SBA-M-50, and (G) SBA-H-50; (II) MCM-41 (A) before and (B−F) after fluorination: (B) MCM-L-RT, (C) MCM-M-RT, (D) MCM-H-RT, (E) MCM-M-50, and (F) MCM-H-50; and (III) CSBA-15 (A) before and (B−E) after treatment: (B) CSBA-L-RT, (C) CSBA-M-RT, (D) CSBA-H-RT, and (E) CSBA-M-50.

however, formation of new surface silanols in this mechanism is not as likely. The detailed characterization results to support these mechanisms are discussed below.

3.1. Structural Analyses. Figure 1 displays the XRD patterns for (I) extracted SBA-15, (II) calcined MCM-41, (III) CSBA-15, and their fluorinated products. The structural data about the materials are also compiled in Table 1.

Table 1. Structural Data of Mesoporous Materials before and after Fluorination

sample[a]	unit cell (Å)[b]	average pore diameter (Å)[c]	BET surface area (m^2/g)	BJH average pore volume (cm^3/g)[c]
SBA-15 (A)	104	74	581	0.44
SBA-M-RT (B)	119	72	527	0.47
SBA-H-RT (C)	111	73	584	0.51
SBA-L-50 (D)	113	85	388	0.55
SBA-M-50 (E)	116	73	578	0.50
SBA-H-50 (F)	106	81	497	0.69
MCM-41 (A)	42	23	991	0.55
MCM-L-RT (B)	43	21	1137	0.51
MCM-M-RT (C)	42	22	1147	0.52
MCM-H-RT (D)	42	21	1053	0.46
MCM-M-50 (E)	43	21	1051	0.64
MCM-H-50 (F)	43	24	1092	0.70
CSBA-15 (A)	119	72	579	0.68
CSBA-15-M-RT (B)	119	78	641	0.81
CSBA-15-H-RT (C)	121	85	675	0.86
CSBA-15-M-50 (D)	119	78	788	0.91

[a] Sample nomenclature (i.e., SBA-15 (A)) to give reference to relating figures. [b] $a_o = 2d_{100}/3^{1/2}$ (Å) for 2D hexagonally ordered materials. [c] Obtained from adsorption branch of the nitrogen adsorption isotherms.

The XRD patterns show that all the materials maintained their ordered mesoporous structures indicating that the fluorination did not result in collapse of the channel walls or the formation of macropores. In fact, as can be seen in Figure 1, fluorination actually resulted in increase in the Bragg reflection peaks of the samples. This may be a result of either pore channel reconstruction into more ordered structures or increase in electron contrast between the channel pores and channel walls upon etching. The latter was a result of the mild etching of the walls of the materials, broadening of the pores (see below). The interplanar spacing of the mesoporous structures did not exhibit significant changes except subtle increases to higher lattice spacing or lattice expansion upon fluorination. The TEM images of the samples also showed that the mesoporous structures of the organic capped and uncapped SBA-15 samples remained intact after fluorination and etching (see the Supporting Information, Figure S1). In the case of the uncapped SBA-15 many of the pore walls appear to be somewhat corrugated, with regions containing irregular bulges, which may be consistent with a broadened pore size distribution and/or increased pore interconnectivity. As will be discussed later, corrugation is also observed to clearly take place on the surface of 250 nm silica nanospheres.

Nitrogen sorption studies were performed to study how the fluorination process altered the surface area, pore diameter and volume, and sorption isotherm (Figure 2 and Table 1). Parent SBA-15 material exhibited ~47 Å pore diameter with a surface area of 581 m^2/g and a pore volume of 0.44 cm^3/g. The isotherm shows sharp capillary condensation step with good hysteresis indicating uniform mesopore size. Upon etching and fluorination, pore volume increases of 7−16% and 14−57% resulted for RT and 50 °C treatments, respectively. BJH pore size distributions generally show a smaller pore size distribution (PSD) for samples fluorinated at RT while a broadening occurs for those fluorinated at 50 °C (see the Supporting

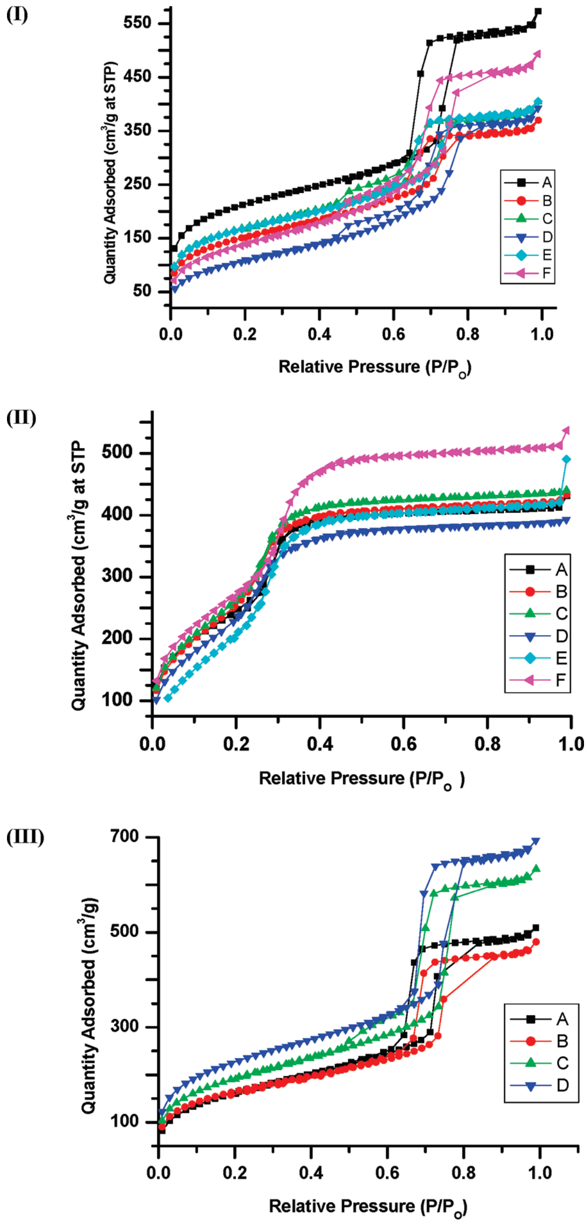

Figure 2. Nitrogen gas adsorption isotherms of mesoporous silica (I) SBA-15 (A) before and (B−F) after its treatment under varying conditions: (B) SBA-M-RT, (C) SBA-H-RT, (D) SBA-L-50, (E) SBA-M-50, and (F) SBA-H-50; (II) MCM-41 (A) before and (B−F) after fluorination: (B) MCM-L-RT, (C) MCM-M-RT, (D) MCM-H-RT, (E) MCM-M-50, and (F) MCM-H-50; and (III) CSBA-15 (A) before and (B-D) after fluorination: (B) CSBA-M-RT, (C) CSBA-H-RT, and (D) CSBA-M-50.

Materials, Figure S2-I). The corresponding isotherms of all fluorinated SBA-15 materials (Figure 2-I) exhibit a shift toward larger partial pressures (P/P_o), showing an enlargement of the primary mesopores. As shown in Figure 2-I, the formation of a tail during the desorption branch, indicative of partial blocking or clogging of the mesopores, also results, proving pore reconstruction in extracted SBA-15 samples leading toward the formation of some restricted mesopores.[16] As shown by PSDs of the materials, RT treatment makes a more highly ordered structure, whereas elevated temperature etches the materials more significantly.

The calcined MCM-41 samples, meanwhile, did not undergo significant changes of isotherm or average pore diameters (Figure 2-II and the Supporting Information, Figure S2-II). Fluorination, in almost all cases, resulted in lowered average diameters, whereas the surface areas and pore volumes were increased by 6−16% and 6−27%, respectively (see the Supporting Information, Figure S2-II). This could be indicative of increased order of the mesopores by possible restructuring of the silicate framework. The only exception is treatment under the highest [BF_4^-] at elevated temperature where the PSD became larger and broadened in a fashion similar to that of SBA-15 series samples.

The HMDS-capped (or CSBA-15) sample exhibits some interesting characteristics after treatment with BF_4^- (Figures 2-III and the Supporting Information, Figure S2-III). The surface area and pore volume increases gradually with increasing [BF_4^-] as well as with increasing temperature. As seen in Table 1, the surface area of the parent CSBA-15 (579 m^2/g) increases to 641, 675, and 788 m^2/g for samples etched with [BF_4^-] concentration of 2.9×10^{-2} M at RT; 5.7×10^{-2} M at RT; and 2.9×10^{-2} M at 50 °C, respectively. The samples with doubled concentration of [BF_4^-] and elevated temperatures showed pore volume increases of 19 − 34%. BJH pore size distributions (see Figure S2-III in the Supporting Information) also showed that as concentration and temperature increased, shifts toward larger diameters and broadened PSDs resulted for the fluorinated samples compared to that of the parent CSBA-15.

The majority of etched materials exhibited larger surface areas than their parent materials. Pore diameter increase in the fluorinated SBA-15 materials may be due to the large density of surface silanols and microprosity of solvent−extracted SBA-15 material and their removal upon fluorination. In the case of the CSBA-15 materials this is due to, as will be shown, desilylation of the TMS capping agents as well as the removal of remaining uncapped silanols upon fluorinaton. A certain extent of pore reconstruction is observed but there is relatively little loss of order or integrity (i.e., pore channel collapse).

3.2. Compositional Analyses. The weight content of trimethylsilyl and silanol species of parent and fluorinated CSBA-15, extracted SBA-15, and calcined MCM-41 materials were obtained from thermogravimetric traces (see the Supporting Information, Table S1 and Figure S3). As can be seen with the CSBA-15 and extracted SBA-15 samples, the overall weight percent loss before and after fluorination is not drastically changed. The TGA profiles of the extracted SBA-15 and its fluorinated samples do show subtle differences, however (see the Supporting Information, Figure S3-I). As can be seen, the extracted materials shows three main regions of weight loss: (1) 25−100 °C, where physisorbed H_2O was removed, (2) 100−400 °C, corresponding to condensation of geminal or closely adjacent silanols participating in H-bonding, and (3) >400 °C where isolated silanols are removed.[8b] Upon fluorination at room temperature or low [BF_4^-] concentration at elevated temperature (50 °C), the second region extends to 450 − 550 °C with steep loss at the end of this region. When higher [BF_4^-] concentrations are used at elevated temperature, the second region extends and experiences a smoother, less steep, weight percent loss. One possible reason for this occurrence may be due to the presence of more unreacted silanols trapped within the mesostructure which would not be reactive during the fluorination process at room temperature or low [BF_4^-] at elevated temperature (50 °C). So, these samples still have higher weight loss in the 450−550 °C region compared to the latter samples whose Si−OH groups were replaced by Si−F. It is seen that some of the fluorinated CSBA-15 samples lose a lower wt% in the organic region than the parent sample (see the Supporting Information, Table S1 and Figure S3-II). This may be attributed to the loss of capping agent during BF_4^- treatment in addition to the reduced number of Si−OH groups due to the capping and subsequent fluorination steps. Nevertheless, the weight percent does not change drastically, because some of the new weight loss may also be due to the presence of residual unreacted silanols trapped within the mesostructure or the loss of certain fluorosilicate species that may have formed (i.e., $(SiO)_1SiF_3$), which condense with nearby silanols.[9d] The loss of these types of species have been shown to occur between 250−350 °C and have similar masses as the capping agent. A slightly steeper weight percent loss over this temperature range for fluorinated CSBA-15 than that of the parent CSBA-15 material is observed. The calcined MCM-41 samples, however, show a marked decrease in silanol (and organic, if any residual surfactant exists) content. During calcination, surface silanols condense to form a more rigid and interconnected Si−O−Si network, which decreases the content of $(SiO)_2-\mathit{Si}(\mathit{OH})_2$ and $(SiO)_3-\mathit{Si}-\mathit{OH}$ species, leading to reduced weight loss from 100 to 600 °C where these silanols condense, expelling H_2O. The weight loss in this region for calcined MCM-41 corresponds to only ~1 wt % (see the Supporting Information, Table S1 and Figure S2-III). Upon fluorination, this value increases to ~4−8 wt %. This weight loss is due to loss of new silanols/ethoxysilanes, HF, and fluorosilicate species that are formed by the fluorination steps. The lowered surface silanol density of calcined materials limits available fluorination sites, inhibiting the mechanism proposed in Scheme 1A, and consequently promotes the second possible pathway (Scheme 1B) where cleavage of siloxane bridges occurs. From the TGA data shown, a general broadening and elongation to higher temperatures of the 100−400 °C implies a lower surface concentration of silanols. Additionally, the higher temperatures necessary for removal of such species proves that the fluorinated materials exhibit enhanced stability and resistance to thermal destruction.

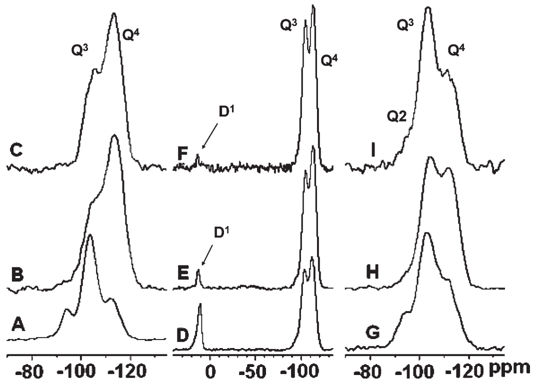

Figure 3. ^{29}Si CP-MAS NMR spectra of (A) SBA-15, (B) SBA-M-RT, (C) SBA-M-50, (D) CSBA-15, (E) CSBA-M-RT, (F) CSBA-M-50, (G) calcined MCM-41, (H) MCM-M-RT, and (I) MCM-M-50.

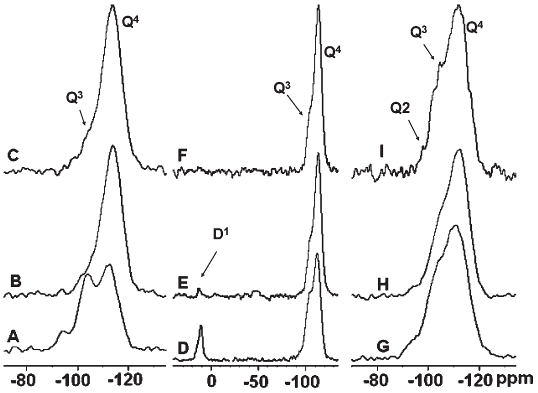

Figure 4. ^{29}Si HP-MAS NMR spectra of (A) SBA-15, (B) SBA-M-RT, (C) SBA-M-50, (D) CSBA-15, (E) CSBA-M-RT, (F) CSBA-M-50, (G) calcined MCM-41, (H) MCM-M-RT, and (I) MCM-M-50.

Using solid-state $^{29}Si\{^1H\}$ cross-polarization magic angle spinning (CP-MAS, Figure 3) and high power magic angle spinning (HP-MAS) NMR spectroscopy (Figure 4), the degree of condensation within the silica framework was determined for samples before and after fluorination. The CP-MAS spectra, when compared to that of the parent materials and their fluorinated products, show many different properties. The spectrum for the parent SBA-15 material (Figure 3A) shows well-defined $(SiO)_2\mathit{Si}(OH)_2$ (Q^2), $(SiO)_3$-$\mathit{Si}OH$ (Q^3), and $(SiO)_4\mathit{Si}$ (Q^4) silicate species, appearing at −94, −103, and −112 ppm, respectively. Upon fluorination (Figure 3B,C), the Q^2 and Q^3 sites are almost completely removed, and a dominant Q^4 peak remains. The Q^4 peak exhibit slightly upfield shifts from −112 to −114 ppm. The spectrum for CSBA-15 parent material (Figure 3D) shows D^1 species at 11 ppm corresponding to the trimethylsilyl (TMS) species (formed from capping with HMDS), Q^3 (−103 ppm), and Q^4 (−112 ppm). Upon fluorination at RT (Figure 3E), D^1 sites are reduced substantially and are almost completely removed at 50 °C (Figure 4F). The Q^3 and Q^4 peaks shift upfield to −105 and −114, respectively. The spectra for MCM-41 (Figures 4G-4I) samples exhibit a trend similar to that of the SBA-15 samples. Well-defined Q^2 (−93 ppm), Q^3 (−103 ppm), and Q^4 (−112 ppm) silicate species can be seen in the parent MCM-41 material. Upon fluorination, the Q^2 peak disappears. The Q^3 and Q^4 species shift upfield to −105 and −113 ppm, respectively, for samples treated BF_4^- at RT and 50 °C. Previously performed studies have reported $(SiO)_2\mathit{Si}(OH)F$ and $(SiO)_2\mathit{Si}F_2$ to correspond to visible signals at −95.5 to −97 ppm and $(SiO)_3\mathit{Si}F$ to be present at −106.5 ppm as well as the formation of pentacoordinated species $(SiO)_4\mathit{Si}F$ and $(SiO)_3\mathit{Si}F_2$ to occur from −118 to −125 ppm.[10a,11c] When these values are compared to the spectra for the fluorinated materials in this study, it is noticed that all spectra exhibit some small intensity contribution from −95 to −100 ppm indicating the possibility of $(SiO)_2\mathit{Si}(OH)F$ and $(SiO)_2\mathit{Si}F_2$ species. Also, in all spectra, the Q^4 peaks baseline at approximately −120 ppm which

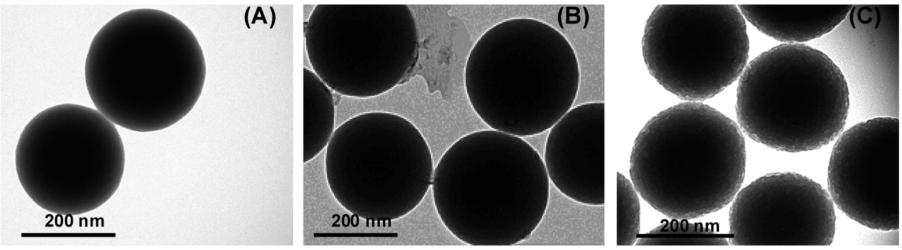

Figure 5. TEM images of silica nanospheres before and after fluorination. Images show (A) silica nanospheres (200 and 500 nm scales), (B) NS-M-RT, and (C) NS-M-50.

implicates the presence of $(SiO)_3\mathit{Si}F$ but not $(SiO)_2\mathit{Si}F_2$. The overall upfield shift of the remaining Q^3 peaks and convergence of signal intensity toward the Q^4 range is evidence of the formation of $(SiO)_3\mathit{Si}F$ species. Additionally, the overall upfield shift of the Q^4 peaks would also provide evidence for the formation of the pentacoordinated species.

As seen in the HP-MAS solid-state NMR spectrum of extracted SBA-15 (Figure 4A), $(SiO)_2\mathit{Si}(OH)_2$ (Q^2), $(SiO)_3\mathit{Si}OH$ (Q^3), and $(SiO)_4\mathit{Si}$ (Q^4) silicate species are present, appearing at −93, −103, and −112 ppm, respectively, with a $(Q^2+Q^3)/Q^4$ ratio of 1.26, indicative of incomplete hydrolysis and condensation of the silanol species during synthesis. Upon fluorination, however, this ratio substantially drops to 0.22 and 0.24 for samples fluorinated at room temperature (Figure 4B) and 50 °C (Figure 4C), respectively, using a 2.9×10^{-2} M Et_3OBF_4 solution. Q^2 and Q^3 species present in the parent material are almost completely removed after fluorination at RT and 50 °C. The fluorinated products exhibit a dominant Q^4 peak that shifts upfield to −114 and −115 ppm for the samples treated at RT and 50 °C, respectively. CSBA-15 samples (Figures 4 D-F) not only showed reduction in the percentage of Q^2 and Q^3 silicates upon fluorination, but also concomitant reduction of D^1 trimethylsilane (TMS) capping species. The ^{29}Si HP-MAS NMR spectrum of CSBA-15 (Figure 4D) exhibited a $(Q^2+Q^3)/Q^4$ ratio of 0.61 and 12% TMS silicate species. Upon fluorination, the $(Q^2+Q^3)/Q^4$ ratio decreases as before, to 0.39 and 0.38 at RT (Figure 4E) and 50 °C (Figure 4F), respectively. A reduction of capped species is also observed in these samples leaving only 2.2 and 0.8% TMS silica sites upon fluorination at RT and 50 °C, respectively, with subsequent decrease in Q^2 and Q^3 indicating fluorination without extensive etching, but rather a more rigid mesostructure, is evidenced. The Q^4 species exhibit the same upfield shift as seen with the extracted SBA-15 samples. Additionally, as shown by BET (see Figure 2-III and the Supporting Information, Figure S2-III), pore reconstruction is shown to occur leading to a more rigid material with a broader PSD than its parent material. ^{29}Si HP-MAS NMR spectra also showed the formation of Q^4 species with upfield shifts from −111 ppm in calcined MCM-41 sample before fluorination to −113 and −114 ppm for its fluorinated samples at RT and 50 °C, respectively. Additionally, the Q^3 region is reduced and slightly shifted upfield from −103 to −106 ppm. The calcined material exhibited a $(Q^2+Q^3)/Q^4$ ratio of 1.07 (Figure 4G), which was reduced to 0.71 and 0.61 after fluorination at RT (Figure 5H) and 50 °C (Figure 4I), respectively.

The ^{29}Si HP-MAS solid-state NMR data presented would be consistent with either increased silica condensation, which is not directly indicated by the small angle XRD or nitrogen gas sorption data, or decrease in surface silanol content due to nucleophilic substitution by fluoride ion. In all cases, the amount of silanol sites is reduced, possibly to a similar degree for the parent materials SBA-15 and CSBA-15. In the CSBA-15 samples desilylation takes place without the formation of new Q^2 and Q^3 silicon sites. The calcined MCM-41 samples most likely did form some amount of new silanols or ethoxysilyl groups from the cleavage/reconstruction of Si−O−Si bonds due to the lack of silanol sites for F^- ions to react with promoting the reaction, with the Q^4 sites being substituted by some fluorinated sites (as shown by TGA). Even though the materials exhibit different TGA profiles and the parent materials have distinctive solid state NMR spectra, there is no immediately discernible differences between the spectra of the final fluorinated OMF analogues whether their parent materials are extracted, capped, or calcined. This is an indication that fluorination of both surface silanols and capping species occurs resulting in products with similar composition when analyzed by TGA and solid state NMR techniques. Therefore, fluorination mainly occurs on the surface of the materials without extensive etching deep within the pore walls unless the surface silanol content is insufficient.

Elemental analyses performed before and after fluorination showed the presence of a substantial concentration of fluorinated species (Table 2). After fluorination, the extracted SBA-15 samples showed the highest F content ranging from 5.0−7.0 wt %, whereas CSBA-15 samples showed a slightly lower loading of 4.0−4.7 wt %, and calcined MCM-41 samples exhibited only 2.4−3.6 wt % F. These results are actually quite high considering the fact that the fluorination process predominantly occurs on the surface of the material by substituting surface silanols (and surface organic groups in case of CSBA-15), indicated by solid state NMR and structural analyses, leading to a material with a very high surface density of silicon oxyfluoride species. These values indicate that these materials contain 1.3−1.9, 2.1−2.5, and 2.6−3.7 mmol/g F for fluorinated MCM-41, CSBA-15, and SBA-15 samples, respectively. Even though MCM-41 has a significantly higher surface area, and is therefore expected to have a larger surface reactivity than the SBA-15 and CSBA-15 materials, the lower values of mmol/g F in the former are not surprising due to

Table 2. Elemental Analysis Results of the Different Mesoporous Samples Studied before and after Fluorination

sample	wt % F[a]	wt % C[b]	wt % H[b]
	SBA-15 Samples		
SBA-15	0.1		
SBA-L-50	5.98		
SBA-M-RT	7.02		
SBA-M-50	5.00		
SBA-H-RT	5.23		
SBA-H-50	5.44		
	MCM-41 Samples		
MCM-41	0.1		
MCM-L-RT	2.56		
MCM-M-50	2.41		
MCM-M-RT	2.79		
MCM-H-50	3.16		
MCM-H-RT	3.61		
	CSBA-15 Samples		
CSBA-15	0.1	9.25	2.08
CSBA-M-RT	4.08	3.29	1.02
CSBA-M-50	4.15	3.55	1.35
CSBA-H-RT	4.68	2.78	0.93

[a] Determined via ion chromatography. [b] Determined via combustion using a Perkin-Elmer 2400 Elemental Analyzer.

its reduced surface silanol concentration and lower content of reactive Q^2 ($(SiO)_2\mathit{Si}(OH)_2$) or Q^3 ($(SiO)_3\mathit{Si}OH$) species resulted because of its calcination. The F loading of the SBA-15 materials compares well with the largest possible amounts of surface organic groups that can be placed on the surface of mesoporous materials, which is often around 4 mmol/g.[40] Typical surface organic density values that can be obtained after postgrafting mesoporous materials with organosilanes is actually ~2 mmol/g,[40] which is well-below the surface fluorine density in our case. Desilylation of TMS capping groups of CSBA-15 upon fluorination clearly evidenced by the marked drop in wt % C and wt % H from 9.25 and 2.08 wt %, respectively, to 2.8−3.6 wt % C and 0.9−1.4 wt % H. The loss of capping agent, however, does not result in production of Q^2 and Q^3 sites, as shown by the ^{29}Si HP-MAS NMR spectra indicating that the fluorination reaction takes place predominantly on the amount of reactive surface sites available. As shown in Table 2, the wt% F of the OMFs is not directly related to changes in neither reaction temperature nor the $[BF_4^-]$ because multiple reaction variations yield similar results with poor correlation. However, the three types of materials do exhibit similar surface fluorination and fluorinated species. These findings, as well, are indications that the concentration of reactive surface sites is the dominating factor.

To investigate the composition of the materials after fluorination and etching, FTIR spectra of the samples were also obtained (see the Supporting Information, Figure S4). As reported extensively, the mesoporous silica materials exhibit a strong, broad absorptions in the 3200−3700 cm^{-1} (Si−OH stretching) and 1000−1200 cm^{-1} (Si−O−Si asymmetric stretching) regions, a weak band at 930−940 cm^{-1} (Si−OH stretching), and a moderate to weak band at 790−800 cm^{-1} (Si−O−Si bending). Upon fluorination, the formation of SiF_x ($x = 1-4$) is expected to yield absorptions from 830 to 1010 cm^{-1} and 450 cm^{-1} corresponding to stretching, bending, and rocking vibrational modes.[2a−c,e] Because of the broad nature of the Si−O−Si stretching mode, however, elucidation of many of these absorptions are clearly difficult due to overlapping. A general broadening of this region is noticed, however, in many of the spectra. Absorptions at 1630 and 1700 cm^{-1} are observed because of the δ_{OH} deformations of physisorbed water. The formation of new ethoxyxilane species on the surface is evidenced by new absorptions at approximately 1370 and 1420 cm^{-1} corresponding to CH_3 δ symmetric, CH_3 δ asymmetric, and CH_2 δ asymmetric stretching modes as well as the formation of new absorptions at 2980 cm^{-1} corresponding to sp^3-hydridized C−H stretching modes.[2f] The formation of a new peak in the 730−750 cm^{-1} region, which was previously assigned to $[F_{6-n}Si(OH)_n]^{2-}$ species,[10] $O_{4/2}\mathit{Si}F$ species, or Si−O−Si stretches altered or polarized by the presence of nearby Si−F species,[14] is also shown to appear in many of the fluorinated SBA-15 samples. As shown by the obtained FTIR spectra, upon fluorination, every fluorinated product exhibits a new band in this region that was not present in the parent materials, CSBA-15, SBA-15, and MCM-41, indicative of new fluorosilicate species within the mesoporous framework.

To further probe the surface properties of these materials, we utilized X-ray photoelectron spectroscopy (XPS) and obtained XPS spectra of SBA-15, CSBA-15, and MCM-41, as well as representative fluorinated species (see the Supporting Information, Figure S5). From the spectra, the composition and degree of fluorination and/or fluorosilicate species formed upon fluorination can be determined by deconvolution of the F1s spectra using a Gaussian distribution function. Upon fluorination, all materials exhibit Si 2p (105−1.07 eV), O 1s (533.3−536.5 eV) and F 1s (683−693 eV) signals consistent with previously reported literature.[7,15] Further careful analysis reveals that two distinct F species are observed at 690.5 and 687.6 eV corresponding to silicon oxyfluoride [$(SiO)_{3-x}\mathit{Si}F_x$] and silicon fluoride (i.e., SiF_4) species, respectively, where the oxyfluoride species is dominant (60−80%). In the case of the CSBA-15 materials (see the Supporting Information, Figure S5D−F), the removal of D^1 species is completed with the same efficiency regardless of reaction temperature. The parent CSBA-15 material is shown to contain 11.2 at % C, which is reduced to 4.2−4.3 at % C upon fluorination in agreement with observations made from the results obtained via solid-state ^{29}Si HP-MAS NMR, nitrogen gas sorption studies (BET and BJH pore size distributions), and elemental analysis.

The etching/fluorination process was also found to form corrugated, or etched, fluorosilica nanospheres (FSNs) upon using silica nanospheres (NS) of 250 ± 10 nm in diameter. These microspheres were characterized before and after treatment with Et_3OBF_4 (Figure 5) by TEM. The TEM images of the silica nanospheres after treatment with a 2.9×10^{-2} M Et_3OBF_4 at RT (Figure 5B) and 50 °C

---

[40] (a) Sharma, K. K.; Asefa, T. *Langmuir* **2008**, *24*, 14306–14320. (b) Sharma, K. K.; Anan, A.; Buckley, R. P.; Ouellette, W.; Asefa, T. *J. Am. Chem. Soc.* **2008**, *130*, 218–228. (c) Sharma, K. K.; Asefa, T. *Angew. Chem., Int. Ed.* **2007**, *46*, 2879–2882.

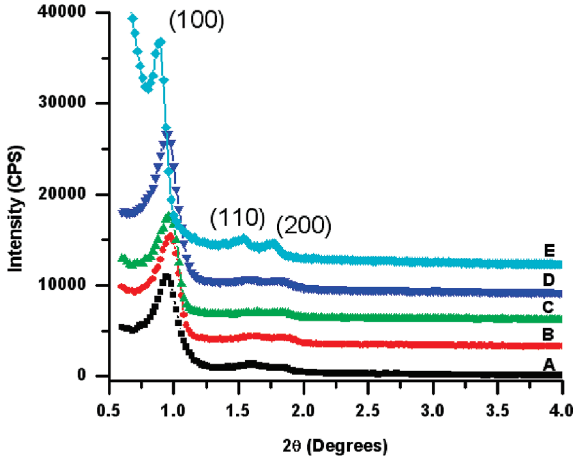

Figure 6. XRD patterns of (A) SBA-15, (B) OMF, (C) SBA-15-SH, (D) SBA-15-SO_3H, and (E) OMF-SO_3H.

Table 3. Structural Data of Mesoporous Epoxidation Catalysts

sample	unit cell (Å)[a]	average pore diameter (Å)[b]	BET surface area (m^2/g)	BJH average pore volume (cm^3/g)[b]
SBA-15 (A)	108	73	860	0.84
OMF (B)	104			
SBA-15-SH (C)	106	70	689	0.72
SBA-15-SO_3H (D)	108	73	702	0.75
OMF-SO_3H (E)	113	73	663	0.79

[a] $a_o = 2d_{100}/3^{1/2}$ (Å) for 2D hexagonally ordered materials. [b] Obtained from adsorption branch of the $N_2(g)$ sorption isotherms.

(Figure 5C) indicated some etching of the surface of the nanoparticles, which is dependent on the etching conditions. As can be seen, no corrugation is shown to result when treatment is performed at RT and the average diameter shows only a slight decrease to 244 ± 13 nm. When the nanospheres are treated at elevated temperature, however, etching of the silica surface is clearly evident and the diameters of these nanospheres are decreased by approximately 13% to 218 ± 8 nm. The latter materials have also exhibited increased wt% F up to ~2 wt %, proving application of the $[BF_4^-]$-based fluorination/etching to nanostructured materials other than mesoporous silicates.

3.3. Catalytic Studies. To test if the fluorination process enhanced the catalytic activity of the Brønsted acid catalyzed ring opening reaction of styrene oxide by aniline forming the corresponding β-amino alcohol, a calcined SBA-15 (weakly acidic) and a sulfonic acid functionalized SBA-15 were prepared. Both materials were subsequently fluorinated at RT using dilute Et_3OBF_4 solution (5.7×10^{-2} M in CH_2Cl_2) forming the corresponding fluorinated solid acids, OMF and OMF-SO_3H, respectively. The materials were characterized by small-angle XRD, nitrogen gas adsorption, TGA, FTIR, XPS, and elemental analyses.

Figure 6 displays the XRD patterns for the $-SO_3H$-functionalized SBA-15, OMF, and OMF-SO_3H materials and their parent samples (calcined and MPTS functionalized SBA-15) used for the synthesis of β-amino alcohols. The structural data is shown in Table 3. As seen with the previously discussed fluorinated SBA-15 and MCM-41 materials, the calcined SBA-15 remains highly ordered after MPTS grafting, oxidation with H_2O_2/H_2SO_4, and subsequent fluorination. All samples exhibit a clearly defined (100) planes as well as higher order (110) and (200) planes. In fact, the OMF-SO_3H catalyst shows more clearly defined (110) and (200) planes than those of the calcined SBA-15 and $-SO_3H$-functionalized parent materials, indicating that the fluorination process leads to pore-reconstruction, yielding a more highly ordered structure in agreement with the other fluorinated materials presented in this paper.

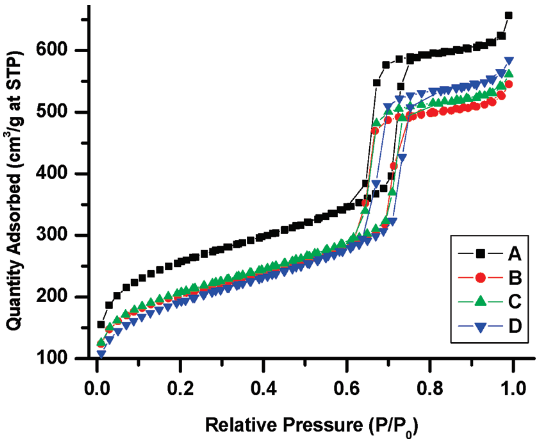

Figure 7. Nitrogen gas adsorption isotherms of (A) SBA-15, (B) SBA-15-SH, (C) SBA-15-SO_3H, and (D) OMF-SO_3H.

Table 4. Chemical Compositions of Solid Acid Catalysts

sample	C (wt %)[a]	H (wt %)[a]	S (wt %)[b]	F (wt %)[b]
SBA-15-SH	3.15	1.45	0.68	
SBA-15-SO_3H	2.31	1.48	0.29	
OMF-SO_3H	2.54	0.80	0.33	2.90

[a] Determined via combustion using a Perkin-Elmer 2400 elemental analyzer. [b] Determined via ion chromatography.

Nitrogen gas adsorption studies were performed to study how the fluorination process altered the surface area, pore diameter and volume, and sorption isotherm of the fluorinated mesoporous catalysts (Figure 7 and Table 3 and the Supporting Information, Figure S6). The parent calcined SBA-15 material used for making the catalysts has a BET surface area of 860 m^2/g and an average pore diameter of 73 Å. The adsorption isotherm shows a sharp capillary condensation step and a very narrow PSD. The SBA-15-SO_3H catalyst shows a slightly lower surface area of 702 m^2/g. Upon fluorination in 5.7×10^{-2} M EtO_3BF_4 at RT, the surface area decreases further to 663 m^2/g, whereas the average pore diameter is slightly broadened but relatively unaltered. As shown in Figure S6 in the Supporting Information, the PSD broadens slightly toward larger diameters. Unlike the extracted SBA-15 samples, where tail formation in the nitrogen adsorption isotherms due to partial pore clogging or bottlenecking is common, fluorination does not lower the integrity of the sulfonic-acid-functionalized calcined SBA-15. The OMF-SO_3H catalyst exhibits an excellent type IV isotherm, void of any substantial pore constrictions. Combined with the small angle XRD data, it is

Scheme 2. Epoxidation of Styrene Oxide with Aniline Forming β-Amino Alcohol Regioisomers, A and B

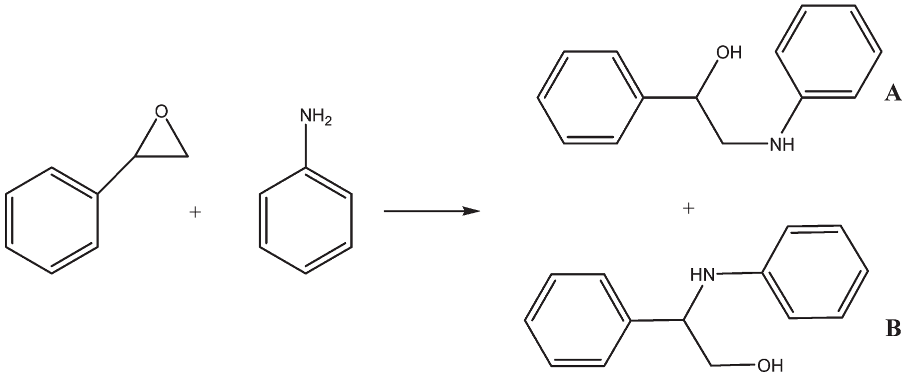

evident that fluorination using this methodology is accomplished predominantly on the surface of the silica while maintaining the overall order and integrity of the catalyst.

The thermogravimetric analysis of the OMF-SO_3H catalyst (see Figure S7 in the Supporting Information) showed significantly more weight loss in the 100 − 600 °C region compared to its nonfunctionalized counterpart (OMF). However, when taking into consideration the propylsulphonic acid groups in the former, the trend in the weight loss due to fluorine species is quite similar. The weight percent losses in the temperature range 100−650 °C for the SBA-15-SH and SBA-15-SO_3H samples are comparable. However, the OMF-SO_3H sample showed slightly higher weight loss in the same temperature range. Elemental analyses (Table 4) were used to determine the concentration of active sulfonic acid catalytic sites to be 0.09 and 0.10 mmol/g for the SBA-15-SO_3H and OMF-SO_3H respectively. The F content of the OMF-SO_3H was found to be 1.5 mmol/g. Upon thiol oxidation there is a significant loss of weight percent sulfur, possibly because of cleavage during oxidation and subsequent washings. Upon fluorination, however, sulfur and the carbon contents are not further reduced, implying that this fluorination methodology does not cause cleavage of immobilized functional groups as seen with surface silanols or capping agents. The presence of fluorine in the OMF-SO_3H sample was further evidenced by FTIR spectroscopy (see the Supporting Information, Figure S8). As can be seen, the fluorinated solid acid catalyst exhibits a peak at 730−750 cm^{-1}, consistent with the previously discussed fluorinated silicas. Because of the low loading content of MPTS, the characteristic -SH stretching band (2575 cm^{-1}), is not seen in the SBA-15-SH material. This signal is usually very weak and barely visible even when the sample exhibits a larger S wt%.[41] XPS (see the Supporting Information, Figure S9) shows that the S 2p of SBA-15 has a binding energy of −163.7 eV. Upon oxidation (SBA-15-SO_3H), this values shifts to −168.5 eV in a manner consistent with previously published data.[42] The fluorinated product, OMF-SO_3H, has a S 2p binding energy which is shifted slightly further to −168.0 eV, which proves that the fluorination process does not alter the sulfonic acid groups. The F 1s peak of OMF-SO_3H has a binding energy of −687.1 eV, which is consistent with that of the fluorinated MCM-41 and SBA-15 samples reported in this work.

The effect of fluorination and etching on the catalytic properties of the materials is investigated with a ring-opening reaction of styrene oxide with aniline forming the corresponding β-amino alcohol (Scheme 2). Control reactions using SBA-15 and thiol (-SH)-modified SBA-15 resulted in percent conversions of 40 and 46%, respectively, whereas SBA-15-SO_3H exhibited 77% conversion at RT (Table 5). Upon fluorination, the resulting fluorinated material (OMF) gave a 79% conversion, which was substantially better than its nonfluorinated counterpart (SBA-15), indicating a higher catalytic activity by OMF compared to its nonfluorinated counterpart (SBA-15). On the other hand, OMF-SO_3H yielded an 87% conversion, a 10% increase from its parent material (SBA-15-SO_3H) (Table 5). As shown, the OMF and OMF-SO_3H catalysts performed competitively with other heterogeneous catalysts while, in our case, using a lower catalyst:reagent ratio of 13 mg:5 mmol (compared to as high as 120 mg:1 mmol in other cases, Table 5) and/or a simplified catalyst synthetic protocol compared to that of materials requiring the incorporation of more expensive metal oxides, metal−chelate complexes, or syntheses requiring metal incorporation in the mesostructure (see Table 5). When the reaction temperature is increased, all three catalysts perform similarly in terms of percent conversion. However, as shown in Table 6, the regioselectivity of the SBA-15-SO_3H is reduced, whereas the fluorinated samples suffer only minor, if any, reduction. Retention of regiochemistry at elevated temperatures may be due to the removal of weakly acidic geminal silanols, leading to a higher overall surface acidity. The fluorination process may form site-isolated catalytic sites by increasing the distance between reactive sites, inhibiting silanol−silanol or silanol−SO_3H hydrogen-bonding interactions and reducing the chances of competition for available reagent. Recyclability studies performed at RT show that reductions in catalytic efficiencies are observed for all three catalysts (Table 7). Loss in catalytic activity may be due to the loss of catalyst between trials, active site leaching, or degradation of the active sites leading to a loss of

---

(41) Saikia, L.; Satyarthi, J. K.; Srinivas, D.; Ratnasamy, P. *J. Catal.* **2007**, *252*, 148–160.

(42) (a) Shen, J. G. C.; Herman, R. G.; Klier, K. *J. Phys. Chem. B* **2002**, *106*, 9976–9978. (b) Shylesh, S.; Sharma, S.; Mirajkar, S. P.; Singh, A. P. *J. Mol. Catal., A: Chem.* **2004**, *212*, 219–228. (c) Shylesh, S.; Samuel, P. P.; Srilakshmi, C.; Parischa, R.; Singh, A. P. *J. Mol. Catal., A: Chem.* **2007**, *274*, 153–158.

Table 5. Comparative Data of Catalytic Efficiency of As-Synthesized Solid Acids and Their Parent Materials

catalyst	epoxide conversion (%)[a]	selectivity (A:B)	time (h)	amine:epoxide ratio (mmol)	catalyst mass (mg)	ref
OMF-SO_3H	87	10: 90	4	5:5	13	this work
OMF	79	10:90	4	5:5	13	this work
$-SO_3H$	77	11:89	4	5:5	13	this work
$-SH$	46	13: 87	4	5:5	13	this work
SBA-15	40	11: 89	4	5:5	13	this work
mesoporous aluminosilicate	70[b]	5: 95	6	1:1	120	30c
AlKIT-5	87[b]	NR[c]	0.5	1:1	50	30b
SBA-15/Co complex	77	11:89	12	100:100	200	31a
Fe-MCM-41	91[b]	NR[c]	4	1:1	NR[d]	31b
$H_{14}[NaP_5W_{29}MoO_{110}]$	92[b]	NR[c]	0.2	5:5	10	32b
Ti-MCM-41	81	6: 94	4	10:10	50	33b, 42c
amberlyst-15	92[b]	NR[c]	2	2:2	100	34
SO_4^{2-}/ZrO_2	97[b]	1: 99	0.75	2:2	60	35
Fe−Zn double metal cyanide	95	2: 98	4	10:10	50	43a
phosphomolybdic acid-Al_2O_3	93[b]	NR[c]	0.5	2:2	200	43b

[a] Determined via GC analysis. [b] Reported as yield (%). [c] Not reported. [d] Authors reported the use of 0.05 mmol of Fe-MCM-41 but did not report the corresponding mass.

Table 6. Influence of Temperature on the Ring Opening of Styrene Oxide with Aniline

catalyst	temp (°C)	time (h)	epoxide conversion (%)	selectivity (A:B)
OMF-SO_3H	22	4	87	10:90
	40	1	91	9:91
		3	94	9:91
	60	1	93	9:91
		3	97	12:88
OMF	22	4	79	10:90
	40	1	84	9:91
		3	95	9:91
	60	1	94	9:91
		3	97	11:89
SBA-15-SO_3H	22	4	77	11:89
	40	1	88	8:92
		3	95	9:91
	60	1	96	16:84
		3	98	16:84

Table 7. Catalyst Recyclability Studies of Synthesized Solid Acids

catalyst	epoxide conversion (%)	selectivity (A:B)
	OMF-SO_3H	
1st run	88	10: 90
2nd run	58	8: 92
3rd run	46	9: 91
4th run	51	9: 91
	OMF	
1st run	81	10: 90
2nd run	66	8: 92
3rd run	50	9:91
4th run	34	8: 92
	$-SO_3H$	
1st run	65	9: 91
2nd run	52	9: 91
3rd run	41	10: 90
4th run	37	9: 91

surface acidity. In addition to be useful as a synthetic tool to create nanomaterials with enlarged pores and fluorinated surface, this method is clearly also proven to be useful to make nanocatalysts with improved catalytic properties.

4. Conclusions

We have developed a facile synthetic etching and fluorination protocol toward the production of highly ordered mesoporous fluorosilicas (OMFs) using dilute concentrations of Et_3OBF_4, a common alkylating reagent, under ambient conditions in a nonaqueous environment. This procedure generally increases the surface area and pore volume of the mesoporous materials. This fluorination and etching method is shown to create a slightly broader pore size distribution and, in some cases, partial pore clogging or bottlenecking. In spite of minor structural changes, however, the materials still retain a highly ordered mesoporous structure as shown by BET, XRD and TEM. It is quite common for functionalized mesoporous silica (FMS) materials formed by postgrafting and postchemical modification techniques to suffer from reductions in surface area, pore diameter and volume, and/or overall porosity. The appearance silicon oxyfluoride (major) and silicon fluoride (minor) species is evidenced by the formation of new peak at 730−750 cm^{-1} in the FTIR spectra. The formation of these species is further identified by characteristic Si−F binding energies in the XPS spectra from 687 to 690 eV. 2.4−7.0 wt % F can be attained with minor variation based upon $[BF_4^-]$ while the type of material used seemed to be a deciding factor. Calcined MCM-41 samples, in spite of higher reactive surface areas, were found to have the lowest wt % F, containing 2.4−3.6 wt %, followed by CSBA-15 samples (4.1−4.7 wt %), and finally the SBA-15 samples, which contained 5.0−7.0 wt % F. Because of the low atomic weight of fluorine and evidence that fluorination predominantly takes place on the surface of the silica, the density (wt %) fluorine obtained is actually very high. Overall, samples containing 5−7 wt % are equivalent to a silica containing 2.6−3.7 mmol/g F, which is mainly present on the silica surface as opposed to doped within the walls. This compares well with the largest possible amounts of organic groups that can be placed on the surface of mesoporous materials, which is often around 4 mmol/g, whereas typical surface organic density values obtained after postgrafting procedures result with organic functionality of ~2 mmol/g,[40] which is well-below the surface fluorine density in our case. The as-described synthetic procedure was also

---

(43) (a) Saikia, L.; Satyarthi, J. K.; Gonnade, R.; Srinivas, D.; Ratnasamy, P. *Catal. Lett.* **2008**, *123*, 24–31. (b) Kumar, S. H.; Leelavathi, P. *J. Mol. Catal., A: Chem.* **2007**, *266*, 65–68.

applied to sulfonic acid ($-SO_3H$) functionalized SBA-15. Enhancement of the acid-catalyzed ring opening of styrene oxide with aniline to produce the corresponding β-amino alcohol was shown. Epoxidation at room temperature after 4 h using $-SO_3H$-functionalized SBA-15 resulted in 77% conversion, whereas the as-synthesized OMF and OMF-SO_3H materials exhibit 79 and 87% conversions, respectively, because of their enhanced solid acid catalytic activity. XPS and elemental analyses serve as proof that this nonaqueous fluorination methodology does not alter the structure of the $-SO_3H$ groups. BET and BJH studies and small-angle XRD confirm that the fluorinated catalyst exhibits larger pore diameter and volume than its precursor as well as increased order. The reported synthetic approach is proven to be versatile as this fluorination and etching method also fluorinates and etches silica nanospheres (FNSs). These findings may give new insights toward the large scale synthesis of mesoporous fluoro- or organofluoro-silica nanomaterials for industrial use in various applications such as silica-based microelectronic devices, nanocatalysts, or materials for chemical separations.

Acknowledgment. We gratefully acknowledge the financial assistance by the U.S. National Science Foundation (NSF), CAREER Grant CHE-0645348 and NSF DMR-0804846, for this work. We thank Dr. Jonathan Shu at Cornell University for his help with XPS measurements and Dave Kiemle at SUNY-ESF for his assistance with solid-state NMR measurements. We also thank Professor Robert A. Bartynski in Physics Department at Rutgers University for valuable discussion regarding XPS data and for offering us an XPS instrument to use.

Supporting Information Available: Transmission electron micrographs, thermogravimetric traces, XPS spectra, and FTIR spectra. This material is available free of charge via the Internet at http://pubs.acs.org.